Revision 1 **Word Count: 6345**

High resolution SIMS U-Th-Pb geochronology of small size (< 5 μm) monazite: Constraints on the timing of Qiuling sediment-hosted gold deposit, South Qinling Orogen, central China

Lei Chen[1*], Albert H. Hofstra[2], Xian-Hua Li[3*], Qiu-Li Li[3], Yu Liu[3], Xiao-Xiao Ling[3], Xiao-Yan Liu[1], Wei Jian[1]

[1] *MNR Key Laboratory for Exploration Theory & Technology of Critical Mineral Resources, China University of Geosciences Beijing, Beijing 100083, China*

[2] *U.S. Geological Survey, MS 973, Denver 80225, USA*

[3] *State Key Laboratory of Lithospheric Evolution, Institute of Geology and Geophysics, Chinese Academy of Sciences, Beijing 100029, China*

*Corresponding author:

E-mail: chenlei1211@cugb.edu.cn, chenlei1211@gmail.com;
lixh@gig.ac.cn

Abstract

Accurately determining the timing of hydrothermal mineralization for the sediment-hosted disseminated gold (SHDG) deposits is difficult because of a lack of both suitable chronometers and *in-situ* techniques with the required spatial resolution and precision. The lack of precise age determinations on gold deposits has hindered understanding of their genesis and relation to the geodynamic setting. The Qinling orogen is one of the most important gold regions in China and contains numerous SHDG deposits. The Qiuling-Jinlongshan deposit is a typical SHDG deposit located in the eastern of the South Qinling Orogen (SQO), with 109 t Au at an average grade of 6.17 g/t. Devonian and Carboniferous metasedimentary rocks host structurally controlled gold mineralization, which is associated with silica-carbonate alteration. Pyrite, arsenopyrite, and arsenian pyrite are major gold carriers and gold also occurs as native gold grains and invisible gold in the sulfides. In this study, the well-defined hydrothermal overgrowth rims (~ 2 μm) of single monazite grains-associated with disseminated auriferous arsenian pyrite and arsenopyrite in low-grade metasedimentary rocks yield U-Pb age of 239 ± 13 Ma (2σ) by high spatial resolution secondary ion mass spectrometry (SIMS). The hydrothermal monazites are cogenetic to the primary gold mineralization where they are closely associated with gold-bearing sulfides. This new age implies that the early to middle Triassic mineralization event in the eastern SQO was related to the Triassic tectonic transition from compression to transpression in the Qinling Orogen after the closure of the Mianlue Ocean. This study highlights 2-μm high spatial resolution SIMS monazite U-Th-Pb dating method as a powerful tool for determining the timing of SHDG deposit worldwide elsewhere. It is crucial to examine monazite textures and its link to hydrothermal alteration before carrying out the isotopic dating of monazite.

Keywords Monazite overgrowth U-Th-Pb dating, SIMS, sediment-hosted gold deposits.

Introduction

Radiometric dating of mineral deposits has critical importance in better understanding ore genesis and associated geological processes, which aids to develop genetic models for successful mineral exploration. However, precise and accurate age constraints on the timing of metal mineralization have long been a big challenge, largely due to the lack of suitable mineral phases that can be unequivocally linked to metal deposition and that have remained closed to isotope diffusion since the time of formation. Sediment-hosted disseminated gold (SHDG) deposits are a significant current source of world gold production (Sillitoe, 2020), mostly including orogenic and Carlin-type gold deposits, typically formed under low-to-mediate temperature, and are featured by very fine-grained alteration assemblages (Hofstra et al. 1999; Muntean et al. 2011). Continuous efforts to precisely date SHDG gold deposits have been made by using various radioactive isotopes methods such as $^{39}Ar/^{40}Ar$ dating of K-bearing silicate minerals (Arehart et al. 1993), Re-Os dating of gold-bearing sulfides minerals (Kerr and Selby, 2012), Rb-Sr dating of galkhaite and illite (Tretbar et al. 2000; Wang et al. 2023), Sm-Nd or U-Pb dating of calcite (Su et al. 2009; Jin et al. 2021), and U-Pb isotopes of U-Th-bearing accessory phases (Vielreicher et al. 2003; Pi et al. 2017; Gao et al. 2024). Notably, recent advances in *in-situ* analytical techniques have promoted age dating of sediment-hosted gold mineralization using U-Th-bearing accessory minerals, because such minerals (e.g., monazite, rutile, xenotime, zircon, apatite) typically have blocking temperatures for U-Pb isotopes significantly higher than the temperature of gold deposition. However, problems remain because (1) in many cases those minerals are too fine relative to the spatial resolution of *in-situ* analysis (e.g., 16 microns for laser ablation) and (2) the minerals may contain multiple generations with some of them have no relation to gold mineralization (e.g., inheritance from the wall rocks). Moreover, many chronometers either are scarce

in these SHDG deposits or are susceptible to isotopic resetting during subsequent metamorphism and deformation events, which makes the reliable ages of many SHDG deposits worldwide still limited. The lack of agreement on the age and tectonic setting for the deposits remains a topic of debate (Cline et al. 2005; Goldfarb and Groves, 2015; Zhao et al. 2021).

Monazite [(Ce, La, Nd, Th)PO_4] commonly contains high U and/or Th, but negligible common Pb and its U-Th-Pb system have closure temperatures greater than 700°C (Parrish, 1990; Williams et al. 2007), which could be highly resistant to weathering and post-ore modifications (Chiaradia et al. 2013). Thus, it has been well-known that monazite is highly suited for isotopic dating (Seydoux-Guillaume et al. 2002; Cherniak et al. 2004). In recent years, the use of hydrothermal monazite for dating gold ore deposits increased markedly, because of the availability of *in-situ* analytical techniques [e.g., secondary ion mass spectrometry (SIMS), sensitive high-resolution ion microprobe (SHRIMP), NanoSIMS, electron probe microanalysis (EPMA), and laser ablation inductively coupled plasma mass spectrometry (LA-ICP-MS)]. The *in-situ* dating of hydrothermal monazite intergrown with ore minerals has successfully constrained the ages of gold deposits worldwide, such as several large orogenic gold deposits in Australia (Brown et al. 2002; McNaughton et al. 2005; Rasmussen et al. 2006; Vielreicher et al. 2010; Fielding et al. 2017), gold deposits of Quadrilátero Ferrífero district in Brazil (Lobato et al. 2007), giant Sukhoi Log SHDG in Russia (Meffre et al. 2008; Yudovskaya et al. 2011), the Hutti gold deposit in southern India (Sarma et al. 2008; Sarma et al. 2011), the gold reefs in the Witwatersrand basin in South Africa (Rasmussen et al. 2007), orogenic gold deposits in Jiaodong gold province eastern China (Deng et al. 2020) and Qinling gold province central China (Yang et al. 2006; Li et al. 2011; Zhao et al. 2019; Qiu et al. 2020; Liu et al. 2021; He, 2022; Zhao et al. 2022; Jian et al. 2024), and many others (Zhou et al. 2019; Yu et al. 2020; Gao et al. 2021; Zhang et al. 2021; Li et al.

2022; Zheng et al. 2022). However, the application of U-Pb geochronology of monazite in SHDG deposits is still hampered by the low temperature alteration assemblages, small grain size, low abundance, and sporadic occurrence, the abundance of mineral inclusions, typically low U and Th contents, common compositional zoning and presence of multi-aged domains (Rasmussen et al. 2001; Rasmussen et al. 2023).

More than 100 SHDG deposits (>2000 t of proven gold reserves) in the South Qinling Orogen (SQO), are hosted in Cambrian to early Triassic marine sedimentary rocks with variable degrees of metamorphism and constitute the second-largest gold province in China (Mao et al. 2002; Chen et al. 2004; Goldfarb et al. 2005; Goldfarb et al. 2014; Liu et al. 2015; Wu et al. 2019). The ages of these gold deposits have been determined by many studies for decades in an attempt to relate the ore-forming episode to the geotectonic evolution of the SQO. Previous geochronologic studies yielded reliable isotopic dates on these gold deposits ranging from 250 to 110 Ma (Table A1), mainly consisting of zircon U-Pb dated igneous rocks crosscutting gold lodes, ore-related mica (sericite/muscovite, biotite, fuchsite) $^{40}Ar/^{39}Ar$, calcite Sm-Nd, sphalerite/pyrite Rb-Sr, and hydrothermal accessory minerals (zircon, monazite, titanite) U-Pb. In several major gold deposits (e.g., Zaozigou, Zhaishang, Ma'anqiao, Qiuling-Jinlongshan), different methods yielded contrasting age results for the same deposits (Zhao et al. 2001; Lu et al. 2006; Zhu et al. 2010; Hua, 2012; Liu et al. 2016; Sui et al. 2018; Qiu et al. 2020; He et al. 2023). Therefore, the timing of gold precipitation in SQO is not well constrained, which hinders our understanding of the exact temporal-spatial gold metallogenic events and genesis of the gold deposit.

The Qiuling-Jinlongshan gold deposit is a large-tonnage and representative SHDG deposit in the eastern SQO with a gold reserve of 109 t at an average grade of 6.17 g/t (Liu, 2006). Our recent study

115 on the Qiuling SHDG deposit found that high grade of 3.63 g/t ores contain disseminated monazite
116 grains. Detailed mineralogical and textural studies have shown that these monazite grains are closely
117 related to auriferous arsenian pyrite and arsenopyrite. These findings make the Qiuling deposit an ideal
118 object for dating the gold mineralization by monazite U-Th-Pb geochronology in SHDG deposits. In
119 this contribution, we show that high spatial resolution (2-μm scale) SIMS U-Th-Pb dating of
120 hydrothermal monazite-(Ce) from Qiuling gold deposit in the SQO can provide timing constraints on
121 representative SHDG mineralization. We present detailed textural and temporal relationships of
122 monazite with gold mineralization, geochemical, and geochronological analyses on the timing of gold
123 mineralization and its potential relationship to tectonic events in the region. Together with previous
124 work, our results confirm that early-middle Triassic gold mineralization in the eastern SQO is more
125 widespread than previous studies.
126
127 **Geological setting**
128 The Qinling orogen is tectonically situated between the North China Craton and South China
129 Block (Fig. 1a; Dong et al. 2011). Traditionally, the Qinling orogen was divided into the North Qinling
130 and South Qinling Orogen (Fig. 1b), which are separated by the Paleozoic Shangdan suture
131 (Ratschbacher et al. 2003; Dong et al. 2011). The North Qinling Orogen consists of an early Paleozoic
132 arc that was accreted to the North China Craton at *ca.* 450 Ma along the Shangdan suture (Meng and
133 Zhang, 2000). This area hosts minor gold mineralization (Mao et al. 2002). The South Qinling Orogen
134 is further subdivided into the northern domain and southern domain along the Zhen'an–Fengxian Fault
135 (Zeng et al. 2012). The northern part of SQO is characterized by a highly deformed basinal flysch
136 sequence (Xue et al. 1996). The southern part of the SQO is covered by Paleozoic strata in the east and

characterized by the easternmost exposure of Triassic turbiditic deposits in the west that are partly calcareous and form part of the immense Songpan–Ganzi Basin (Fig. 1b; Mao et al. 2002). The Paleozoic and Triassic sedimentary rocks were intensely deformed during the Qinling orogeny, and along with this, numerous regional northwestern striking folds and thrust faults were also produced (Li et al. 2020). These faults are the first control on the distribution of the gold deposits in the SQO (Mao et al. 2002; Chen and Santosh, 2014), and most of which are hosted in Devonian rocks composed of carbonate, siliciclastic and argillaceous rocks with a total thickness of *ca.* 3000–8000 m that were deposited in several extensional fault-bounded basins (Liu and Yang, 1990).

The Qiuling-Jinlongshan gold deposit is situated in the northern part of the Zhen'an Basin of the SQO (Fig. 2a), which is an EW-trending rift basin formed during the opening of the Mianlue Ocean at the Early to Middle Devonian (Hu et al. 2002; Dong and Santosh, 2016; Cheng et al. 2019). Previous studies have elaborated on the ore deposit geology, structural characteristics, fluid inclusions, and H-O-S-Pb isotopes of the Qiuling-Jinlongshan SHDG deposits (Zhang et al. 2000; Zhao and Feng, 2002; Zhao et al. 2005; Zhang et al. 2006; Chen et al. 2015; Li et al. 2020; Ma et al. 2020). The main host horizon for the gold deposit is a turbiditic sequence of fine-grained sandstone, siltstone-silty shale, calcareous siltstone, and limestone of the Upper Devonian Nanyangshan Formation (D3n) that contains about 90% of the Au reserve (Fig. 2b). Siltstone, intercalated with silty shale, is the important ore-bearing host. Another horizon, representing about 10% of the Au ore, is in the Carboniferous Yuanjiagou Formation (C1y) and consists of cherty, banded limestone that is intercalated with silty shale, silty sandstone, argillaceous limestone, and calcareous shale (Fig. 2b). There are no exposures of igneous rocks in the mine area. Hydrothermal alteration types associated with Au occurrences in the Qiuling-Jinlongshan gold deposit area include silicification and calcite as replacements and veinlets

159 with lesser veinlets of pyrite, arsenopyrite, barite, and kaolinite, although no systematic zonation has
160 been documented. Gold ores are closely related to silicate and pyrite. Gold ore characteristically is
161 massive, banded, brecciated, and present in veinlets and disseminations (Fig. 3a), but also developed in
162 mesoscopic fracture networks. Stages of ore genesis most likely began with replacement or
163 precipitation of 0.5– to 2–mm-thick, or less, pyrite and arsenopyrite along bedding (S0) layers (Fig. 3b),
164 which also contain sporadic As-rich, zoned pyrite (Fig. 4). Invisible gold in disseminated in very
165 fine-grained arsenian pyrite and arsenopyrite, low-temperature alteration assemblages, and has a
166 geochemical association of Au-As-Hg-Sb-(Tl) (Chen et al. 2015). Gold mineralization is dominated by
167 dissemination of fine-grained auriferous pyrite and arsenopyrite in carbonaceous shales and siltstones,
168 with minor amounts of veinlets composed of coarse-grained pyrite, arsenopyrite, and quartz.
169

170 ## Samples and analytical methods

171 ### Sample preparation

172 The monazite-bearing ore sample (QL105, Fig. 3a), from the No. 304 ore body comprising
173 high-grade banded As-pyrite and arsenopyrite gold ores, containing 3.63 g/t Au, has been studied in
174 detail. This sample is representative ore in the Qiuling gold deposit, consisting of quartz, mica, calcite,
175 ankerite, pyrite, arsenopyrite, and calcite with minor monazite. The sample was prepared as a polished
176 thin section and was examined under optical microscopy to characterize the mineralogy and textures of
177 monazite. After petrographic examination, the sample was investigated using scanning electron
178 microscopy (SEM) to characterize the morphological and textural features of monazite grains (Figs.
179 3b-c). Then, the thin section was cut out with a diamond wire saw and mounted in 25-mm-diameter
180 epoxy discs together with pieces of monazite standards for SIMS U-Th-Pb dating (Figs. 3d and e). The

discs were polished to produce a smooth, flat sample surface with relief of less than a few μm, which is critical for high-accuracy, high-precision isotope ratio analysis by SIMS and compositional analysis by EPMA.

Textural and compositional analysis

SEM investigation was carried out at the Institute of Geology, Chinese Academy of Geological Sciences, using an FEI NOVA nanoSEM equipped with an Oxford X-Max 50 detector. The sample was coated with a 250 Å carbon film and then imaged using SEM with secondary electron imaging (SEI) and back-scattered electron (BSE) modes. The EDAX GENESIS energy-dispersive spectroscopy (EDS) was performed using an accelerating voltage of 15 kV and a working distance of 15 mm.

The mineral/phase distribution map and the mineral proportions (vol.%) were determined for the thin section (whole domains) of the QL105 sample using a TESCAN integrated mineral analyser (TIMA) at Nanjing Hongchuang Geological Exploration Technology Service Company, Limited, China. The TIMA comprises a Mira-3 scanning electron microscope equipped with four EDS (EDAX Element 30). The measurements were performed at an acceleration voltage of 25 kV, a probe current of 9 nA, a working distance of 15 mm, a pixel spacing of 3 μm, and a dot spacing of 9 μm; the scanning time was 6 h. The current and BSE signal intensity was calibrated on a platinum Faraday cup using the automated procedure. The EDS performance was checked using a manganese standard. The samples were scanned using the TIMA liberation analysis module.

EPMA wavelength-dispersive X-ray spectrometry (WDS) analysis and elemental mapping were applied to reveal the internal texture and chemistry variation of the monazite grains. All analyses were performed using a JEOL JXA-iSP100 EPMA at the Nanjing Hongchuang Geological Exploration

Technology Service Company. An accelerating voltage of 15 kV was used for monazite. The spot beam diameter was 1~2 μm. Higher current gave the optimal count rate for trace elements and excitation of less intense analytical lines such as REE. The EPMA was calibrated by natural and synthetic standards (Table A2). Details on EPMA settings for WDS analysis are available in Table A2. The content of the elements in the mineral formula is expressed in atoms per formula unit (apfu). The formula of monazite was normalized on 4 oxygen atoms. The probe current of 500 nA was for elemental mapping. The step size for elemental mapping was 0.5 μm, and the dwell time was set to 200 ms for each step/pixel.

SIMS U-Th-Pb dating of monazite

In-situ monazite SIMS U-Th-Pb dating was conducted using a Cameca IMS1280HR ion microprobe at the Institute of Geology and Geophysics, Chinese Academy of Sciences in Beijing. The instrument description and operating protocol applied to monazite have been detailed by Li et al. (2013). A primary beam of O^- was focused to a size of $<$ 3 μm on the monazite surface with an intensity of ca. 0.2 nA. Monazite RW-1 ($^{207}Pb/^{235}U$ age=904.15 ± 0.26 Ma [2σ], Th=11.8 ± 1.0 wt% [2σ], and Th/ U=42.5 ± 3.0 [2σ]; Ling et al. 2017) was interspersed with unknowns as the standard to calibrate U and Th concentrations and U-Th-Pb isotope ratios. To choose the exact location of different Th concentrations from the single monazite grain, the image of $^{232}Th^{16}O_2$ signals was set up (Fig. 3f). A repeatability of 1.5% (1σ RSD) was derived from the long-term $^{206}Pb/^{238}U$ measurement of the monazite standard. As a measure of the accuracy of SIMS U-Th-Pb monazite analyses calibrated against RW-1 standard, in-house monazite M6 was employed as a secondary standard. A concordia age of 484.7 ± 14 Ma (2σ RSD) is obtained for monazite M6 (Table A4), which agrees with the recommended value, within errors (unpublished). For monazite SIMS analysis, the ^{204}Pb-based

common Pb correction is inappropriate because of large analytical uncertainty owing to low ^{204}Pb concentrations and the probability of isobaric interferences derived from $^{232}Th^{144}Nd^{16}O_2^{2+}$ (Ireland et al. 1999; Li et al. 2013). Therefore, a ^{207}Pb-based correction (Williams, 1997; Li et al. 2013) was done to subtract common Pb (initial Pb) using the terrestrial Pb isotope composition for the corresponding ages (Stacey and Kramers, 1975). Age calculations and plots were performed with the ISOPLOT add-in (Ludwig, 2012).

Results

Monazite occurrence

The sample QL105 is composed of quartz (66 vol.%), mica (26 vol.%), ankerite (3.2 vol.%), arsenopyrite (1.7 vol.%), pyrite (1.5 vol.%), biotite (0.7 vol.%), and calcite (0.7 vol.%). Monazite is heterogeneously distributed in this sample (red marked spots in Fig. 3d). Monazite is small in size (3 to 30 μm) and euhedral to subhedral in shape (Figs. 3c and 4). Although monazite grains appear to be rather homogeneous optically, they frequently show strong zonation in BSE imaging (Fig. 5). The zoning pattern revealed by SEM is concentric zonation. Monazite I occur particularly abundant in metamorphosed fine-grained sandstone and interbedded siltstones from the Nanyangshan Formation (Fig. 4a). The monazite grains occur as isolated, clustered, and beaded crystals in ankerite and quartz (Fig. 4), are commonly elongate and parallel with the slaty cleavage (Fig. 4a). Most cores appear to be compositionally homogeneous in BSE images (Fig. 4). The cores are clearly visible in high-contrast BSE images, and typically form more than 50% of the entire crystal, delineated by a bright rim zone (typically < 3 μm) of monazite, which in places, contains minute specks of a Th-rich silicate mineral (Fig. 4b). Within a single sample, monazite cores range in shape from broadly oval to highly irregular

247 with scalloped and embayed outlines (Fig. 5). The core-rim boundary of some of the more complete
248 and unaltered cores is irregular with serrated outlines in places (Fig. 5).

249 Monazite II with 'intergrowth-like' zonation coexists with arsenopyrite in strongly altered and
250 mineralized belts of the Nanyangshan Formations (Fig. 3b). The grain is small euhedral and skeletal
251 crystals and their intergrowths incorporated into auriferous sulfides (Fig. 4c), as inclusions in pyrite
252 (Figs. 4d-g), and some form rims on sulfides (Figs. 4h, i and 6b).

253

254 **Monazite chemistry**

255 One hundred and three electron microprobe analytical spots were measured on thirty-seven
256 monazite crystals. Both generations of monazite are characterized by a heterogeneous internal structure
257 with markedly varying concentrations of particular REEs and Th (Figs. 5 and 6; Table A3). They are
258 rich in LREE, with Ce predominant, and are depleted in HREE (contents are below the detection limit
259 of microprobe). The chemical compositions of monazite make up a continuous series with Ce_2O_3
260 contents from 26.99 to 35.20 wt.%. The La_2O_3 and Nd_2O_3 contents vary also continuously from 7.86 to
261 20.65 wt.% and 7.18 to 19.94 wt.%, respectively. The La–Ce, and La–Nd correlation coefficients are
262 0.21 and –0.74, respectively. Therefore, Ce monazite can be enriched in both La and Nd, whereas Nd
263 monazite is always depleted in La (Fig. 6a). Their P_2O_5 contents range from 26.94 wt.% to 30.65 wt.%.
264 Minor proportions of CaO (0.03 to 1.31 wt.%) and SiO_2 (0.01 to 2.44 wt.%) were also detected. The U
265 and Pb contents are below the detection limit of the microprobe.

266 X-ray element maps for U, Th, La, Ca, and Y of monazite grains reveal several distinct
267 compositional differences between the cores and rims (Fig. 5). The cores have higher concentrations of
268 Th, U, Y, and Ca, and lower concentrations of La, than the rims (Table A3). Monazite II differs from

monazite I in lower ThO_2 and lower Y contents. Monazite I is characteristically high in Th content (>1.34 wt.%), and Th/Ce ratio (>0.05), and is typical of high-temperature igneous and metamorphic monazite (Fig. 6b). Monazite II is more enriched in LREE than Monazite I (Fig. 6c). Monazite II is characteristically low in Th content (<1 wt.%) and Th/Ce ratio (<0.04), which is characteristic of hydrothermal monazite (Fig. 6b). Calcium is incorporated into monazite by the brabantite substitution, and there is a strong correlation between Ca and Th in both the cores and the rims of the monazite crystals. It is notable that there is a negative correlation between (Th + U + Si) (apfu) and (REE + Y + P) (apfu) (Fig. 6d), indicating that Th^{4+} is charge-balanced through the coupled substitutions of $Th4^{+}$ + $Ca^{2+} = 2(REE + Y)^{3+}$ and $Th^{4+} + Si^{4+} = P^{5+} + (REE + Y)^{3+}$. Many of the grains contain minute specks (<1 μm) with high Th contents. Qualitative analysis of the Th-rich inclusions by EDS indicates that they also contain Si, suggesting that the mineral may be huttonite or possibly thorite.

Monazite U-Th-Pb ages

In-situ SIMS U-Th-Pb results of monazite are provided in Table A5. Three analyses were made on the core of monazite II. The $^{206}Pb/^{238}U$ dates are 1763 Ma, 738.6 Ma, and 597.5 Ma, respectively. The core of monazite II has high U (1777–11186 ppm) and Th (35880–75594 ppm), resulting in low Th/U ratios (7–23). The remaining 20 analyses of monazite II plot close to the concordant line yielded a lower intercept $^{206}Pb/^{238}U$ age of 245 ± 13 Ma (2σ, MSWD = 0.93; Fig. 7a) on a Tera-Wasserburg plot. After applying the ^{207}Pb-based correction for common Pb, the weighted mean $^{206}Pb/^{238}U$ age was 239 ± 13 Ma (2σ, MSWD = 0.73; Fig. 7b). The rim of monazite contains highly variable U (18–581 ppm) and Th (2,604–58607 ppm), with Th/U ratios of 18 to 1677. In Fig. 7c, the common-Pb corrected $^{208}Pb/^{232}Th$ age ranged from 216 ± 13 Ma (2σ) to 406 ± 14 Ma (2σ).

Discussion

Formation of the monazite from ore zones

The crystal textures and occurrence of monazite, in combination with mineral geochemistry, can be used to confidently distinguish monazite of different origins (Vielreicher et al. 2003; Rasmussen and Muhling, 2007; Williams et al. 2007; Taylor et al. 2015; Zi et al. 2019). These cores of monazite in the Qiuling gold deposit have a wide range of U-Pb ages that are obviously older than those of the rims of monazite (Fig. 7a), which suggests that the core of monazite was originally introduced into the sedimentary rocks as detritus. The ages of the cores overlap with the ages of detrital zircon grains from the same locality (Dong and Santosh, 2016). We, therefore, propose that the core of monazite is likely detrital in origin. The cores of monazite crystal have a large range of ThO_2 (1.52 to 9.68 wt.%) and show concentric zoning with respect to ThO_2 (Fig. 6b). This confirms the metamorphic source for the detrital grains.

Some monazite crystals occur in contact with auriferous sulfides and are concentrated within small areas (Fig. 4), which is different from the more sparsely and homogeneously distributed magmatic or metamorphic monazite. The rims of monazite crystals have low contents of ThO_2 (<1 wt%, Fig. 6b). Indeed, the irregular, scalloped core-rim contact (Fig. 5a) provides strong textural evidence for the partial dissolution of former detrital monazite cores by post-depositional fluids, consistent with experimental results (e.g. Teufel and Heinrich, 1997; Seydoux-Guillaume et al. 2002). All these features fit the criteria of hydrothermal monazite as proposed by Schandl and Gorton (2004) and suggest that the rims of monazite grew synchronously with and/or slightly post-dated the texturally associated sulfides. Our study shows that detrital Th-rich monazite is unstable during hydrothermal

313 fluid activity, and undergoes replacement via dissolution and reprecipitation, forming relatively low-Th
314 monazite overgrowths with trace amounts of $ThSiO_4$ inclusions (Rasmussen and Muhling, 2007). The
315 presence of minute thorium silicate inclusions in the hydrothermal monazite rims suggest that Th
316 released by dissolution of the detrital monazite core was immobile and could not all be accommodated
317 in the hydrothermal monazite rims, which suggests that the dissolution of the cores was closely linked
318 in time to the growth of the hydrothermal rims (Fig. 4b).

319 The dissolution and replacement were not isochemical: some elements (e.g. LREE) were added
320 while others (e.g. Ca, Th, U, and Y) were removed. The differences in composition between the detrital
321 monazite cores and the hydrothermal monazite rims, probably reflect the chemical environment under
322 which the new monazite formed. The preservation of detrital monazite cores in the composite crystals
323 suggests that the conditions (e.g. temperature, fluid composition, flow rate) required for complete
324 replacement of all of the detrital cores were not sustained over a sufficiently long period of time. X-ray
325 mapping and WDS analysis show that formed metamorphic detrital monazite contains significantly less
326 LREE than the outer part of the rim (Fig. 5). The outer, broader part of the rim contains significantly
327 more LREE, which rises slightly toward the crystal margin, indicating a pattern of LREE enrichment
328 during hydrothermal monazite growth. It's widely accepted that CO_2 can promote the solubility of REE
329 since CO_3^{2-} forms strong complexes with the REE (e.g., Wood, 1990; Williams-Jones et al. 2000;
330 Hetherington et al. 2010). The much lower Th and higher LREE concentrations of hydrothermal
331 monazite indicate that the solubility of Th^{4+} is relatively low compared to that of $LREE^{3+}$ in
332 hydrothermal fluids responsible for monazite precipitation (Deng et al. 2020). This may result from the
333 fact that thorium tends to be immobile in low temperature, aqueous-carbonic metamorphic fluids
334 (Schandl and Gorton, 2004). Primary fluid inclusion studies indicate ore-forming fluid in the Qiuling

deposit has low homogenization temperatures (120–277°C), low salinity (5.7–8.6 wt.% NaCl eqv), and low CO_2 content (0.89–5.41 mol.%; Zhang et al. 2002). This study presents an example of monazite compositional alteration and resetting of U-Pb ages caused by dissolution-reprecipitation reactions, which are induced by low to moderate salinity carbon-aqueous fluids at low temperatures (i.e., < 300°C). Since these fluids are commonly involved in the formation of orogenic gold deposits (e.g., Groves et al. 1998; Goldfarb et al. 2005), the U-Pb ages of these monazite crystals record the timing of gold mineralization.

Chemical disturbance and Th-Pb age scattering of monazite

Most chemical variations observed in the Qiuling monazites could be explained by the huttonite ($ThSiO_4$) and brabantite [$CaTh(PO_4)_2$] exchanges (Fig. 6d), which have been attributed to hydrothermal alteration processes (Poitrasson et al. 1996, 2000). Intra-grain variations of the Th content in distinct age and chemical domains (Fig. 5) are a good indication of interaction with fluids. In some natural hydrothermal monazites from sericitized samples, Poitrasson et al. (2000) have observed strong removal of Th leading to the overgrowth of Th-poor domains. This variable behavior of Th during fluid-rock interactions may explain its heterogeneous distribution as well as its variable relations with Y in the Qiuling monazites. In most grains, Th decrease correlates with Th-Pb age decrease from core to rim (Fig. 7d). Experiments have shown that Ca-rich fluids can enhance monazite dissolution and result in the recrystallization of grains with strong chemical modifications (Seydoux-Guillaume et al. 2002). The main host horizon for the Qiuling gold deposit is a turbiditic sequence of fine-grained sandstone, siltstone-silty shale, calcareous siltstone, and limestone of the Upper Devonian Nanyangshan Formation. Chen et al. (2015) analyzed sulfur isotopes of ore-stage pyrite associated with monazite in

357 the Qiuling gold deposit and demonstrated a relatively narrow range of positive $\delta^{34}S$ values, ranging
358 from 8.1‰ to 15.2‰, and suggested the ore-forming fluid was derived from metamorphic
359 devolatilization of Paleozoic marine sedimentary rocks. Hence, in the case of the Qiuling gold deposit,
360 it is not surprising that fluid interactions were able to induce a significant scattering of the monazite
361 Th-Pb ages (Fig. 7c).
362
363 **Timing of hydrothermal gold mineralization in the Qiuling deposit and its implications**
364 Hydrothermal mineralization at the Qiuling SHDG deposit, however, has been difficult to date
365 directly due to a lack of both suitable chronometers and *in-situ* techniques with the required spatial
366 resolution and precision. The age of the Qiuling deposit has not been well-constrained. Previous
367 hydrothermal calcite Sm-Nd dating results of fine-grain calcite vein in the Qiuling deposit yielded ages
368 of 232.3 ± 4.3 Ma (Hua, 2012). Moreover, the sericite $^{40}Ar/^{39}Ar$ dating results of the ore sample yielded
369 ages of 232.7 ± 6.9 Ma (Zhao et al. 2001) and 142.3 ± 0.8 Ma (Liu et al. 2016), respectively. The
370 interpretations of the geological significance of these ages, however, are questionable. For example, the
371 formation of some dated minerals (e.g., sericite and calcite) may not be coeval with gold deposition.
372 One of the $^{40}Ar/^{39}Ar$ plateau ages of sericite is much younger than that of the other in the Qiuling
373 deposit. The sericite has low-closure temperatures (Chiaradia et al. 2013), suggesting its isotopic
374 system could be easily reset during later hydrothermal events. In fact, post-ore calcite and/or quartz
375 veins are widely developed in the Qiuling deposit. It is very likely that these post-ore fluids have reset
376 Ar-Ar isotopic systems. Consequently, a more precise dating method of a syn-mineralization mineral is
377 urgently needed to confine the timing of gold mineralization of the Qiuling deposit. It is, therefore,
378 necessary to evaluate the reliability of our age. The paragenesis of the minerals indicates that fine-grain

379 pyrite and arsenopyrite are closely related to native gold and monazite in the disseminated ore (Figs.
380 4d-i). Abundant invisible gold precipitation is observed in this stage, which is indicated by pyrite and
381 arsenopyrite LA-ICP-MS results (Hua et al. 2012; Chen et al. 2015). Monazite grains were also
382 observed to be closely associated with auriferous pyrite and arsenopyrite in the sulfide band (Fig. 3b),
383 and thus coeval with the main gold mineralization. Indeed, visible gold precipitation is also observed in
384 this stage (Fig. 4c). We thus conclude that the hydrothermal monazite growth is coeval with main gold
385 deposition and our monazite U-Pb geochronological result is, therefore, a reliable age to define the
386 Qiuling gold mineralization. The 20 spot analyses of hydrothermal monazite growth from the Qiuling
387 gold deposit yielded a weighted mean ^{207}Pb-based corrected ^{206}Pb/^{238}U age of 239 ± 13 Ma (2σ,
388 MSWD = 0.73), indicating that the Qiuling gold mineralization occurred at ~239 Ma.

389 Our U-Pb ages of hydrothermal monazite in the Qiuling deposit show that there was a significant
390 episode of gold mineralization in the early to middle Triassic in the eastern SQO, which is more
391 widespread than previously thought in the western SQO (Table A1 and Fig. 8; *ca.* 248-238 Ma in the
392 Xiahe-Hezuo district; Jin et al. 2017; Sui et al. 2018; Yu et al., 2020a; Yu et al., 2020b). The Qiuling
393 gold mineralization can be classified as orogenic gold deposits (discussed above and in Chen et al.
394 2015). The gold sources of the orogenic gold deposits in the SQO have been proposed mainly from
395 Paleozoic sediments during Triassic orogeny and metamorphism, especially Devonian and Triassic
396 sediments (Zeng et al. 2012; Chen et al. 2015; Ma et al. 2018; Wu et al. 2018; Qiu et al. 2020).
397 Moreover, a relatively extensional regime has been widely accepted as important for the upwelling of
398 deeply sourced fluid and the precipitation of orogenic gold deposits (Chen et al. 2004; Large et al. 2011;
399 Goldfarb and Groves, 2015). Hence, the new geochronology results presented in this study (~239 Ma)
400 support a model in which the ultimate control of the gold mineralization in the Zhen'an basin is the

Triassic tectonic transition in the geodynamic setting from compression to transpression in the Qinling orogen after the closure of the Mianlue Ocean (Mao et al. 2012).

Implications

This study demonstrates that monazite could record early hydrothermal events, and not be affected by later hydrothermal alteration. Considering the high closure temperature of monazite, a full reset of the U-Pb system seems unlikely. It is crucial to examine the monazite textures and recognize alteration textures before carrying out isotopic dating of monazite collected from SHDG deposits. During the alteration of hydrothermal monazite that typically contains low Th concentrations and incorporation of common Pb through coupled dissolution-reprecipitation reactions. These features can be identified under high-contrast BSE images but are not always visible in reflected-light photomicrograph images. Without prior compositional and textural characterization, the hydrothermal growth rim could be easily neglected. Attempts to date the core of monazite crystals could yield mixed age information and meaningless ages. Our study presents an example of monazite compositional alteration and the 2-μm scale hydrothermal monazite growth of U-Th-Pb ages caused by coupled dissolution-reprecipitation reactions, which are induced by low salinity and CO_2 aqueous fluids at low temperatures are commonly involved in the formation of SHDG deposits. This paper contributes to this area of geological science at the junction between geochronology and economic geology. From the methodological point of view, this study illustrates high resolution SIMS U-Th-Pb geochronology of small size (< 5 μm) monazite can be achieved. It has potential applications in dating precious samples or multistage geological events, as well as revealing the detailed growth history of monazite by image U-Th-Pb acquisition. Monazites have long been recognized in many sediment-hosted gold deposits worldwide elsewhere (Table A6),

423 such as Sukhoi log gold deposit in the Siberian craton (Russia; Meffre et al., 2008; Yakubchuk et al.,
424 2014), gold deposits in the Telfer area of the Paterson Province (Australia; Rowins et al., 1997;
425 Schindler et al., 2016), and gold deposits in the Muruntau area in the Tian Shan orogenic belt
426 (Uzbekistan; Bierlein and Wilde, 2010; Kempe et al. 2015). Thus, the common presence of monazite
427 closely associated with native gold in many SHDG deposits makes 2-μm scale hydrothermal monazite
428 growth a potential robust U-Pb geochronometer for gold mineralization, especially in the SHDG
429 deposit without suitable geochronometers to record the hydrothermal process.
430

431 **Acknowledgements**

432 We thank Hong-Xia Ma and Jiao Li for their help with the microanalytical sample preparation. We
433 appreciate Jian-Wei Li, Shu-Guang Hua, Xin-Hui Liu, Gen-Min Li, and Tuan-Wei Liu for their help in
434 the field. The manuscript benefited from detailed and constructive reviews by one anonymous reviewer
435 and Dr. Xiao-Ping Xia, which are gratefully appreciated. We thank the editor professor Fang-Zhen
436 Teng for editorial handling and useful suggestions. This study was supported by the National Key R&D
437 Program of China (2018YFA0702600) and the Natural Science Foundation of China (Grant 41672092).
438

439 **Compliance with Ethical Standards**

440 The authors declare that they have no conflict of interest. This article does not contain any studies
441 with human or animal subjects.
442

443 **REFERENCES**

444 Arehart, G.B., Foland, K.A., Naeser, C.W., and Kesler, S.E. (1993) $^{40}Ar/^{39}Ar$, K/Ar, and fission track geochronology of
445 sediment-hosted disseminated gold deposits at Post-Betze, Carlin Trend, northeastern Nevada. Economic Geology, 88,
446 622-646.

Bierlein, F.P., and Wilde, A.R. (2010) New constraints on the polychronous nature of the giant Muruntau gold deposit from wall-rock alteration and ore paragenetic studies. Australian Journal of Earth Sciences, 57, 839-854.

Brown, S. M., Fletcher, I. R., Stein, H. J., Snee, L. W., and Groves, D. I. (2002) Geochronological constraints on Pre-, Syn-, and postmineralization events at the world-class Cleo gold deposit, eastern goldfields province, western Australia. Economic Geology, 97, 541-559.

Chen, L., Li, X. H., Li, J. W., Hofstra, A. H., Liu, Y., and Koenig, A. E. (2015) Extreme variation of sulfur isotopic compositions in pyrite from the Qiuling sediment-hosted gold deposit, West Qinling orogen, central China: an in situ SIMS study with implications for the source of sulfur. Mineralium Deposita, 50, 643-656.

Chen, Y. J., Zhang, J., Zhang, F. X., Pirajno, F., and Li, C. (2004) Carlin and Carlin-like gold deposits in western Qinling mountains and their metallogenic time, tectonic setting and model. Geological Review, 50, 134-152 (in Chinese with English abstract).

Chen, Y. J., and Santosh, M. (2014) Triassic tectonics and mineral systems in the Qinling Orogen, central China. Geological Journal, 49, 338-358.

Cheng, C., Li, S. Y., Xie, X. Y., Manger, W. L., and Busbey, A. B. (2019) Pb detrital zircongeochronology and Hf isotopic composition of Permian clastic rocks, Zhen'an basin, South Qinling belt: Implications for the Paleozoic tectonic evolution of the Qinling orogenic belt. International Geology Review, 61, 1462-1478.

Cherniak, D. J., Zhang, X. Y., Nakamura, M., and Watson, E. B. (2004) Oxygen diffusion in monazite. Earth and Planetary Science Letters, 226, 161-174.

Chiaradia, M., Schaltegger, U., Spikings, R., Wotzlaw, J. F., and Ovtcharova, M. (2013) How accurately can we date the duration of magmatic-hydrothermal events in porphyry systems?–An invited paper. Economic Geology, 108, 565-584.

Cline, J. S., Hofstra, A. H., Muntean, J. L., Tosdal, R. M., and Hickey, K. A. (2005) Carlin-type gold deposits in Nevada: Critical geologic characteristics and viable models, *in* Hedenquist, J. W., Thompson, J. F. H., Goldfarb, R. J., and Richards, J. P., eds., One Hundredth Anniversary Volume, Society of Economic Geologists, 451-484.

Deng, J., Qiu, K. F., Wang, Q. F., Goldfarb, R., Yang, L. Q., Zi, J. W., Geng, J. Z., and Ma, Y. (2020) In situ dating of hydrothermal monazite and implications for the geodynamic controls on ore formation in the Jiaodong gold province, eastern China. Economic Geology, 115, 671-685.

Dong, Y., and Santosh, M. (2016) Tectonic architecture and multiple orogeny of the Qinling Orogenic Belt, Central China. Gondwana Research, 29, 1-40.

Dong, Y., Zhang, G., Neubauer, F., Liu, X., Genser, J., and Hauzenberger, C. (2011) Tectonic evolution of the Qinling orogen, China: Review and synthesis. Journal of Asian Earth Sciences, 41, 213-237.

Fielding, I. O. H., Johnson, S. P., Zi, J. W., Rasmussen, B., Muhling, J. R., Dunkley, D. J., Sheppard, S., Wingate, M. T. D., and Rogers, J. R. (2017) Using in situ SHRIMP U-Pb monazite and xenotime geochronology to determine the age of orogenic gold mineralization: An example from the Paulsens mine, Southern Pilbara craton. Economic Geology, 112, 1205-1230.

Gao, W., Hu, R., Hofstra, A. H., Li, Q., Zhu, J., Peng, K., Mu, L., Huang, Y., Ma, J., and Zhao, Q. (2021) U–Pb dating on hydrothermal rutile and monazite from the Badu gold deposit supports an early Cretaceous age for Carlin-type gold mineralization in the Youjiang basin, southwestern China. Economic Geology, 116, 1355-1385.

Gao, W., Hu, R., Huang, Y., Zhu, J., Li, Q., Mei, L., Bi, X., and Liu, J. (2024) Hydrothermal apatite as a robust U–Th–Pb chronometer for the Carlin-type gold deposits in the Youjiang basin, SW China. Mineralium Deposita, 59, 109-131.

Goldfarb, R. J., and Groves, D. I. (2015) Orogenic gold: Common or evolving fluid and metal sources through time. Lithos, 233, 2-26.

Goldfarb, R. J., Baker, T., Dubé, B., Groves, D. I., Hart, C. J. R., and Gosselin, P. (2005) Distribution, character, and genesis of gold deposits in metamorphic terran, *in* Hedenquist, J. W., Thompson, J. F. H., Goldfarb, R. J., and Richards, J. P., eds., One Hundredth Anniversary Volume, Society of Economic Geologists, 407-450.

Goldfarb, R. J., Taylor, R. D., Collins, G. S., Goryachev, N. A., and Orlandini, O. F. (2014) Phanerozoic continental growth and gold metallogeny of Asia. Gondwana Research, 25, 48-102.

Groves, D. I., Goldfarb, R. J., Gebre-Mariam, M., Hagemann, S. G., and Robert, F. (1998) Orogenic gold deposits: A proposed classification in the context of their crustal distribution and relationship to other gold deposit types. Ore Geology Reviews, 13, 7-27.

He, C. G. (2022) Geology, mineralization, and genesis of typical gold deposits in the northern belt of the West Qinling Orogen: Dissertation, The China University of Geosciences (Wuhan) (in Chinese with English abstract).

He, C. G., Li, J. W., Kontak, D. J., Jin, X. Y., Wu, Y. F., Hu, H., Zu, B., Yu, X. L., Zhao, S. R., and Du, S. (2023) An Early Cretaceous gold mineralization event in the Triassic west Qinling orogen revealed from U-Pb titanite dating of the Ma'anqiao gold deposit. Science China Earth Sciences, 66, 316-333 (in Chinese with English abstract).

Hetherington, C. J., Harlov, D. E., and Budzyń, B. (2010) Experimental metasomatism of monazite and xenotime: mineral stability, REE mobility and fluid composition. Mineralogy and Petrology, 99, 165-184.

Hofstra, A. H., Snee, L. W., Rye, R. O., Folger, H. W., Phinisey, J. D., Loranger, R. J., Dahl, A. R., Naeser, C. W., Stein, H. J., and Lewchuk, M. T. (1999) Age constraints on Jerritt Canyon and other carlin-type gold deposits in the Western United States; relationship to mid-Tertiary extension and magmatism. Economic Geology, 94, 769-802.

Hu, J. M., Meng, Q. R., Bai, W. M., Zhao, G. C. (2002) Mid-Late Paleozoic extension of the Wudang block in the South Qinling tectonic belt, China. Geological Bulletin of China, 21, 471-477 (in Chinese with English abstract).

Hua, S. G. (2012) Mineralogy, geochemistry, and geochronology of the Qiuling gold deposit, Zhen'an County, Shanxi Province: Dissertation, The China University of Geosciences (Wuhan) (in Chinese with English abstract).

Hua, S. G., Wang, L. J., Jia, X. F., Chen, L., and Li, J. W. (2012) Occurrence and enrichment mechanism of gold in the Qiuling Carlin-type gold deposit, Zhen'an County, Shaanxi Province, China. Earth Science, 37, 989-1002 (in Chinese with English abstract).

Ireland, T., Wooden, J., Persing, H., and Ito, B. (1999) Geological applications and analytical development of the SHRIMP-RG. Eos (Transactions, American Geophysical Union), 80, F1117.

Jian, W., Mao, J., Lehmann, B., Wu, S., Chen, L., Song, S., Xu, J., Wang, P., and Liu, J. (2024) Two discrete gold mineralization events recorded by hydrothermal xenotime and monazite, Xiaoqinling gold district, central China. American Mineralogist, 109, 73-86.

Jin, X. Y., Li, J.W., Hofstra, A. H., and Sui, J. X. (2017) Magmatic-hydrothermal origin of the early Triassic Laodou lode gold deposit in the Xiahe-Hezuo district, west Qinling orogen, China: implications for gold metallogeny. Mineralium Deposita, 52, 883-902.

Jin, X., Zhao, J., Feng, Y., Hofstra, A.H., Deng, X., Zhao, X., and Li, J. (2021) Calcite U-Pb dating unravels the age and hydrothermal history of the giant Shuiyindong Carlin-type gold deposit in the Golden Triangle, south China. Economic Geology, 116, 1253-1265.

Kempe, U., Seltmann, R., Graupner, T., Rodionov, N., Sergeev, S.A., Matukov, D.I., and Kremenetsky, A.A. (2015) Concordant U–Pb SHRIMP ages of U-rich zircon in granitoids from the Muruntau gold district (Uzbekistan): Timing of intrusion, alteration ages, or meaningless numbers. Ore Geology Reviews, 65, 308-326.

Kerr, A., and Selby, D. (2012) The timing of epigenetic gold mineralization on the Baie Verte Peninsula, Newfoundland, Canada: new evidence from Re–Os pyrite geochronology. Mineralium Deposita, 47, 325-337.

Large, R. R., Maslennikov, V. V., Robert, F. O., Danyushevsky, L. V., and Chang, Z. (2007) Multistage sedimentary and metamorphic origin of pyrite and gold in the giant Sukhoi Log deposit, Lena gold province, Russia. Economic Geology, 102, 1233-1267.

Li, N., Chen, Y. J., Fletcher, I. R., and Zeng, Q. T. (2011) Triassic mineralization with Cretaceous overprint in the Dahu Au–Mo deposit, Xiaoqinling gold province: Constraints from SHRIMP monazite U–Th–Pb geochronology. Gondwana Research, 20, 543-552.

Li, Q. L., Li, X. H., Lan, Z. W., Guo, C. L., Yang, Y. N., Liu, Y., and Tang, G. Q. (2013) Monazite and xenotime U–Th–Pb geochronology by ion microprobe: dating highly fractionated granites at Xihuashan tungsten mine, SE China. Contributions to Mineralogy and Petrology, 166, 65-80.

Li, R., Chen, H., Large, R. R., Zhao, L., Liu, Y., Jiao, J., Xia, X. P., and Yang, Q. (2020) Ore-forming fluid source of the orogenic gold deposit: Implications from a combined pyrite texture and geochemistry study. Chemical Geology, 552, 119781.

Li, X. H., Fan, H. R., Xie, H. L., Yang, K. F., Hollings, P., Wei, Z. H., Zhu, R. X., Zeng, Q. D., Liang, G. Z., and Wu, J. J. (2022) Geochronology, ore-forming processes and fluid sources of the Qinglonggou gold deposit, North Qaidam (NW China): Constraints from in-situ U-Pb dating of monazite and geochemistry of pyrite. Ore Geology Reviews, 149, 105093.

Ling, X. X., Huyskens, M. H., Li, Q. L., Yin, Q. Z., Werner, R., Liu, Y., Tang, G. Q., Yang, Y. N., and Li, X. H. (2017) Monazite RW-1: a homogenous natural reference material for SIMS U–Pb and Th–Pb isotopic analysis. Mineralogy and Petrology, 111, 163-172.

Liu, B., and Yang, Z. (1990) Devonian sedimentary environments and basin evolution in Zhashui-Zhen'an district, East Qinling. China, 8, 3-12.

Liu, J., Liu, C., Carranza, E. J. M., Li, Y., Mao, Z., Wang, J., Wang, Y., Zhang, J., Zhai, D., Zhang, H., Shan, L., Zhu, L., and Lu, R. (2015) Geological characteristics and ore-forming process of the gold deposits in the western Qinling region, China. Journal of Asian Earth Sciences, 103, 40-69.

Liu, J., Wang, Y., Mao, J., Jian, W., Huang, S., Hu, Q., Wei, R., and Hao, J. (2021) Precise ages for lode gold mineralization in the Xiaoqinling gold field, southern margin of the North China Craton: New constraints from in situ U-Pb dating of hydrothermal monazite and rutile. Economic Geology, 116, 773-786.

Liu, X. H (2006) Potential reserve prediction of Jinlongshan gold deposit. Contributions to Geology and Mineral Resources Research, 21(S1), 118-120 (in Chinese with English abstract).

Liu, Y. H., Li, Z., Zhou, S., and Han, Y. X. (2016) Geological characteristics, ore forming ages and geological significance of Donggou-Jinlongshan gold deposit, South Qinling belt. Earth Science Frontiers, 23, 81 (in Chinese with English abstract).

Lobato, L. M., Santos, J. O. S., McNaughton, N. J., Fletcher, I. R., and Noce, C. M. (2007) U–Pb SHRIMP monazite ages of the giant Morro Velho and Cuiabá gold deposits, Rio das Velhas greenstone belt, Quadrilátero Ferrífero, Minas Gerais, Brazil. Ore Geology Reviews, 32, 674-680.

Lu, Y., Li, H., Chen, Y., and Zhang, G. (2006) $^{40}Ar/^{39}Ar$ dating of alteration minerals from Zhaishang gold deposit in Minxian County, Gansu Province, and its geological significance. Mineral Deposits, 25, 590-597 (in Chinese with English abstract).

Ludwig, K. (2012) User's manual for Isoplot version 3.75–4.15: A geochronological toolkit for Microsoft Excel. Berkeley Geochronological Center Special Publication 5: Publication, v. 5.

Ma, J., Lü, X., Escolme, A., Li, S., Zhao, N., Cao, X., Zhang, L., and Lu, F. (2018) In-situ sulfur isotope analysis of pyrite from the Pangjiahe gold deposit: Implications for variable sulfur sources in the north and south gold belt of the South Qinling orogen. Ore Geology Reviews, 98, 38-61.

Ma, Y., Zhu, L., Lu, R., Ding, L., Zhang, G., Xiong, X., and Li, B. (2020) Geology and in-situ sulfur and lead isotope analyses of the Jinlongshan Carlin-type gold deposit in the Southern Qinling Orogen, China: Implications for metal sources and ore genesis. Ore Geology Reviews, 126, 103777.

Mao, J., Qiu, Y., Goldfarb, R. J., Zhang, Z., Garwin, S., and Fengshou, R. (2002) Geology, distribution, and classification of gold deposits in the western Qinling belt, central China. Mineralium Deposita, 37, 352-377.

Mao, J. W., Zhou, Z. H., Feng, C. Y., Wang, Y. T., Zhang, C. Q., Peng, H. J., and Yu, M. (2012) A preliminary study of the Triassic large-scale mineralization in China and its geodynamic setting. Geology in China, 39, 1437-1471 (in Chinese with English abstract).

McNaughton, N. J., Mueller, A. G., and Groves, D. I. (2005) The age of the giant golden Mile deposit, Kalgoorlie, western

Australia: Ion-microprobe zircon and monazite U-Pb geochronology of a synmineralization lamprophyre dike. Economic Geology, 100, 1427-1440.

Meffre, S., Large, R. R., Scott, R., Woodhead, J., Chang, Z., Gilbert, S. E., Danyushevsky, L. V., Maslennikov, V., and Hergt, J. M. (2008) Age and pyrite Pb-isotopic composition of the giant Sukhoi Log sediment-hosted gold deposit, Russia. Geochimica et Cosmochimica Acta, 72, 2377-2391.

Meng, Q. R., and Zhang, G. W. (2000) Geologic framework and tectonic evolution of the Qinling orogen, central China. Tectonophysics, 323, 183-196.

Muntean, J. L., Cline, J. S., Simon, A. C., and Longo, A. A. (2011) Magmatic-hydrothermal origin of Nevada's Carlin-type gold deposits. Nature Geoscience, 4, 122-127.

Parrish, R. R. (1990) U-Pb dating of monazite and its application to geological problems. Canadian Journal of Earth Sciences, 27, 1431-1450.

Pi, Q., Hu, R., Xiong, B., Li, Q., and Zhong, R. (2017) In situ SIMS U–Pb dating of hydrothermal rutile: reliable age for the Zhesang Carlin-type gold deposit in the golden triangle region, SW China. Mineralium Deposita, 52, 1179-1190.

Poitrasson, F., Chenery, S., and Bland, D. J. (1996) Contrasted monazite hydrothermal alteration mechanisms and their geochemical implications. Earth and Planetary Science Letters, 145, 79-96.

Poitrasson, F., Chenery, S., and Shepherd, T. J. (2000) Electron microprobe and LA-ICP-MS study of monazite hydrothermal alteration: Implications for U-Th-Pb geochronology and nuclear ceramics. Geochimica et Cosmochimica Acta, 64, 3283-3297.

Qiu, K. F., Yu, H. C., Deng, J., McIntire, D., Gou, Z. Y., Geng, J. Z., Chang, Z. S., Zhu, R., Li, K. N., and Goldfarb, R. (2020) The giant Zaozigou Au-Sb deposit in West Qinling, China: magmatic- or metamorphic-hydrothermal origin? Mineralium Deposita, 55, 345-362.

Rasmussen, B., Fletcher, I. R., and McNaughton, N. J. (2001) Dating low-grade metamorphic events by SHRIMP U-Pb analysis of monazite in shales. Geology, 29, 963-966.

Rasmussen, B., Fletcher, I. R., Muhling, J. R., Mueller, A. G., and Hall, G. C. (2007) Bushveld-aged fluid flow, peak metamorphism, and gold mobilization in the Witwatersrand basin, South Africa: Constraints from in situ SHRIMP U-Pb dating of monazite and xenotime. Geology, 35, 931-934.

Rasmussen, B., Sheppard, S., and Fletcher, I. R. (2006) Testing ore deposit models using in situ U-Pb geochronology of hydrothermal monazite: Paleoproterozoic gold mineralization in northern Australia. Geology, 34, 77-80.

Rasmussen, B., Zi, J. W., and Muhling, J. R. (2023) Tectonic fluid expulsion: U-Pb evidence for punctuated hydrothermal fluid flow and hydraulic fracturing during orogenesis. Earth and Planetary Science Letters, 604, 117997.

Ratschbacher, L., Hacker, B. R., Calvert, A., Webb, L. E., Grimmer, J. C., McWilliams, M. O., Ireland, T., Dong, S., and Hu, J. (2003) Tectonics of the Qinling (Central China): tectonostratigraphy, geochronology, and deformation history. Tectonophysics, 366, 1-53.

Rowins, S. M., Groves, D. I., McNaughton, N. J., Palmer, M. R., and Eldridge, C. S. (1997) A reinterpretation of the role of granitoids in the genesis of Neoproterozoic gold mineralization in the Telfer Dome, Western Australia. Economic Geology, 92, 133-160.

Sarma, D. S., Fletcher, I. R., Rasmussen, B., McNaughton, N. J., Mohan, M. R., and Groves, D. I. (2011) Archaean gold mineralization synchronous with late cratonization of the Western Dharwar Craton, India: 2.52 Ga U-Pb ages of hydrothermal monazite and xenotime in gold deposits. Mineralium Deposita, 46, 273-288.

Sarma, D. S., McNaughton, N. J., Fletcher, I. R., Groves, D. I., Mohan, M. R., and Balaram, V. (2008) Timing of gold mineralization in the Hutti gold deposit, Dharwar craton, south India. Economic Geology, 103, 1715-1727.

Schandl, E. S., and Gorton, M. P. (2004) A textural and geochemical guide to the identification of hydrothermal monazite: Criteria for selection of samples for dating epigenetic hydrothermal ore deposits. Economic Geology, 99, 1027-1035.

Schindler, C., Hagemann, S. G., Banks, D., Mernagh, T., and Harris, A. C. (2016) Magmatic hydrothermal fluids at the

sedimentary rock-hosted, intrusion-related Telfer gold-copper deposit, Paterson orogen, Western Australia: Pressure-temperature-composition constraints on the ore-forming fluids. Economic Geology, 111, 1099-1126.

Seydoux-Guillaume, A. M., Paquette, J. L., Wiedenbeck, M., Montel, J. M., and Heinrich, W. (2002) Experimental resetting of the U–Th–Pb systems in monazite. Chemical Geology, 191, 165-181.

Sillitoe, R. H. (2020) Gold Deposit Types: An Overview, *in* Sillitoe, R. H., Goldfarb, R. J., Robert, F., and Simmons, S. F., eds., Geology of the World's Major Gold Deposits and Provinces, Society of Economic Geologists, 23, 1-28.

Stacey, J. S., and Kramers, J. D. (1975) Approximation of terrestrial lead isotope evolution by a two-stage model. Earth and Planetary Science Letters, 26, 207-221.

Su, W., Hu, R., Xia, B., Xia, Y., and Liu, Y. (2009) Calcite Sm–Nd isochron age of the Shuiyindong Carlin-type gold deposit, Guizhou, China. Chemical Geology, 258, 269-274.

Sui, J. X., Li, J. W., Jin, X. Y., Vasconcelos, P., and Zhu, R. (2018) $^{40}Ar/^{39}Ar$ and U-Pb constraints on the age of the Zaozigou gold deposit, Xiahe-Hezuo district, West Qinling orogen, China: Relation to early Triassic reduced intrusions emplaced during slab rollback. Ore Geology Reviews, 101, 885-899.

Taylor, R. J. M., Clark, C., Johnson, T. E., Santosh, M., and Collins, A. S. (2015) Unravelling the complexities in high-grade rocks using multiple techniques: the Achankovil Zone of southern India. Contributions to Mineralogy and Petrology, 169, 51.

Teufel, S., and Heinrich, W. (1997) Partial resetting of the U-Pb isotope system in monazite through hydrothermal experiments: An SEM and U-Pb isotope study. Chemical Geology, 137, 273-281.

Tretbar, D.R., Arehart, G.B., and Christensen, J.N. (2000) Dating gold deposition in a Carlin-type gold deposit using Rb/Sr methods on the mineral galkhaite. Geology, 28, 947-950.

Vielreicher, N.M., Groves, D.I., Fletcher, I.R., McNaughton, N.J., and Rasmussen, B. (2003) Hydrothermal monazite and xenotime geochronology: A new direction for precise dating of orogenic gold mineralization. SEG Discovery, 1-16.

Vielreicher, N. M., Groves, D. I., Snee, L. W., Fletcher, I. R., and McNaughton, N. J. (2010) Broad synchroneity of three gold mineralization styles in the Kalgoorlie gold field: SHRIMP, U-Pb, and $^{40}Ar/^{39}Ar$ geochronological evidence. Economic Geology, 105, 187-227.

Wang, R., Wang, Q., Zhao, J., Groves, D.I., Kirkland, C.L., Feng, Y., Uysal, I.T., Yang, L., and Deng, J. (2023) Carbonate U–Pb and illite Rb–Sr geochronology of sediment-hosted gold: A case study of Yata gold deposit. Chemical Geology, 621, 121352.

Williams, I. S. (1997) U-Th-Pb geochronology by ion microprobe, Applications of Microanalytical Techniques to Understanding Mineralizing Processes, 7, Society of Economic Geologists.

Williams, M. L., Jercinovic, M. J., and Hetherington, C. J. (2007) Microprobe monazite geochronology: Understanding geologic processes by integrating composition and chronology. Annual Review of Earth and Planetary Sciences, 35, 137-175.

Williams-Jones, A. E., Samson, I. M., and Olivo, G. R. (2000) The genesis of hydrothermal fluorite-REE deposits in the Gallinas mountains, New Mexico. Economic Geology, 95, 327-341.

Wood, S. A. (1990) The aqueous geochemistry of the rare-earth elements and yttrium: 2. Theoretical predictions of speciation in hydrothermal solutions to 350°C at saturation water vapor pressure. Chemical Geology, 88, 99-125.

Wu, Y. F., Li, J. W., Evans, K., Koenig, A. E., Li, Z. K., O'Brien, H., Lahaye, Y., Rempel, K., Hu, S. Y., Zhang, Z. P., and Yu, J. P. (2018) Ore-Forming processes of the Daqiao epizonal orogenic gold deposit, West Qinling Orogen, China: Constraints from textures, trace elements, and sulfur isotopes of pyrite and marcasite, and raman spectroscopy of carbonaceous material. Economic Geology, 113, 1093-1132.

Wu, Y. F., Li, J. W., Evans, K., Vasconcelos, P. M., Thiede, D. S., Fougerouse, D., and Rempel, K. (2019) Late Jurassic to Early Cretaceous age of the Daqiao gold deposit, West Qinling Orogen, China: implications for regional metallogeny. Mineralium Deposita, 54, 631-644.

Xue, F., Lerch, M. F., Kröner, A., and Reischmann, T. (1996) Tectonic evolution of the East Qinling Mountains, China, in the

667 Palaeozoic: a review and new tectonic model. Tectonophysics, 253, 271-284.
668 Yang, R. S., Chen, Y. J., Zhang, F. X., Li, Z. H., Mao, S. D., Liu, H. J., and Zhao, C. H. (2006) Chemical Th-U-Pb ages of
669 monazite from the Yangshan gold deposit, Gansu province and their geologic and metallogenic implications. Acta
670 Petrologica Sinica, 22, 2603-2610 (in Chinese with English abstract).
671 Yakubchuk, A., Stein, H., and Wilde, A. (2014) Results of pilot Re–Os dating of sulfides from the Sukhoi Log and Olympiada
672 orogenic gold deposits, Russia. Ore Geology Reviews, 59, 21-28.
673 Yu, B., Zeng, Q., Frimmel, H. E., Qiu, H., Li, Q., Yang, J., Wang, Y., Zhou, L., Chen, P., and Li, J. (2020) The 127 Ma gold
674 mineralization in the Wulong deposit, Liaodong Peninsula, China: Constraints from molybdenite Re-Os, monazite
675 U-Th-Pb, and zircon U-Pb geochronology. Ore Geology Reviews, 121, 103542.
676 Yu, H. C., Qiu, K. F., Nassif, M. T., Geng, J. Z., Sai, S. X., Duo, D. W., Huang, Y. Q., and Wang, J. (2020a) Early orogenic gold
677 mineralization event in the West Qinling related to closure of the Paleo-Tethys Ocean – Constraints from the
678 Ludousou gold deposit, central China. Ore Geology Reviews, 117, 103217.
679 Yu, H. C., Qiu, K. F., Sai, S. X., McIntire, D. C., Pirajno, F., Duo, D. W., Miggins, D. P., Wang, J., Jia, R. Y., and Wu, M. Q.
680 (2020b) Paleo-tethys late triassic orogenic gold mineralization recorded by the Yidi'nan gold deposit, West Qinling,
681 China. Ore Geology Reviews, 116, 103211.
682 Yudovskaya, M. A., Distler, V. V., Rodionov, N. V., Mokhov, A. V., Antonov, A. V., and Sergeev, S. A. (2011) Relationship
683 between metamorphism and ore formation at the Sukhoi Log gold deposit hosted in black slates from the data of
684 U-Th-Pb isotopic SHRIMP-dating of accessory minerals. Geology of Ore Deposits, 53, 27-57.
685 Zeng, Q., McCuaig, T. C., Hart, C. J. R., Jourdan, F., Muhling, J., and Bagas, L. (2012) Structural and geochronological studies
686 on the Liba goldfield of the West Qinling Orogen, Central China. Mineralium Deposita, 47, 799-819.
687 Zhang J, Chen YJ, Zhang FX, and Li C. (2002) Geochemical study of ore fluid in Jinlongshan Carlin-type gold ore belt in
688 southwestern Shaanxi province. Miner Deposits, 21, 283-291 (in Chinese with English abstract).
689 Zhang, F., Chen, Y., Li, C., Zhang, J., Ma, J., and Li, X. (2000) Geological and geochemical character and genesis of the
690 Jinlongshan-Qiuling gold deposits in Qinling orogen: Metallogenic mechanism of the Qinling-pattern Carlin-type
691 gold deposits. Science in China Series D: Earth Sciences, 43, 95-107.
692 Zhang, H. D., Liu, J. C., and Fayek, M. (2021) Multistage mineralization in the Haoyaoerhudong gold deposit, Central Asian
693 Orogenic Belt: Constraints from the sedimentary-diagenetic and hydrothermal sulfides and gold. Geoscience Frontiers,
694 12, 587-604.
695 Zhang, J., Chen, Y., Zhang, F., and Li, C. (2006) Ore fluid geochemistry of the Jinlongshan Carlin-type gold ore belt in Shaanxi
696 Province, China. Chinese Journal of Geochemistry, 25, 23-32.
697 Zhao, H., Wang, Q., Groves, D. I., and Deng, J. (2021) Progressive spatial and temporal evolution of tectonic triggers and
698 metasomatized mantle lithosphere sources for orogenic gold mineralization in a Triassic convergent margin:
699 Kunlun-Qinling Orogen, central China. GSA Bulletin, 133, 2378-2392.
700 Zhao, L. Q., Chen, X., Zhou, H., and Li, X. M. (2001) Metallogenic epoch of Jinlongshan micro-fine disseminated gold deposit,
701 South Qinling Mountains. Chinese Journal of Geology, 36, 489-489 (in Chinese with English abs.).
702 Zhao, L., and Feng, Z. (2002) Control of favorable lithology on Jinlongshan micro-fine disseminated gold deposits, southern
703 Qinling Mountains. Science in China Series D: Earth Sciences, 45, 123-132.
704 Zhao, L., Deng, J., Chen, X., Zhou, H., and Li, X. (2005) Structural control to the genesis of sediment-hosted disseminated
705 Jinlongshan gold orebelt, China. Resource Geology, 55, 9-19.
706 Zhao, S. R., Li, J. W., Lentz, D., Bi, S. J., Zhao, X. F., and Tang, K. F. (2019) Discrete mineralization events at the Hongtuling
707 Au-(Mo) vein deposit in the Xiaoqinling district, southern North China Craton: Evidence from monazite U-Pb and
708 molybdenite Re-Os dating. Ore Geology Reviews, 109, 413-425.
709 Zhao, S. R., Li, J. W., McFarlane, C. R. M., Robinson, P. T., Li, Z. K., Wu, Y. F., Zhao, X. F., He, C. G., Kang, X., and Chen, C. Y.
710 (2022) Recognition of late Paleoproterozoic gold mineralization in the North China craton: Evidence from

multi-mineral U-Pb geochronology and stable isotopes of the Shanggong deposit. GSA Bulletin, 135, 211-232.

Zheng, J., Shen, P., and Feng, W. (2022) Hydrothermal monazite trumps rutile: Applying U-Pb geochronology to evaluate complex mineralization ages of the Katbasu Au-Cu deposit, Western Tianshan, Northwest China. American Mineralogist, 107, 1201-1215.

Zhou, H., Sun, X., Wu, Z., and Huang, Q. (2019) Timing of skarn gold deposition in the giant Beiya polymetallic gold deposit, southwest China: Constraints from in situ monazite SIMS U-Th-Pb geochronology. Ore Geology Reviews, 106, 226-237.

Zhu, L., Zhang, G., Lee, B., Guo, B., Gong, H., Kang, L., and Lü, S. (2010) Zircon U-Pb dating and geochemical study of the Xianggou granite in the Ma'anqiao gold deposit and its relationship with gold mineralization. Science China Earth Sciences, 53, 220-240.

Zi, J. W., Rasmussen, B., Muhling, J. R., Maier, W. D., and Fletcher, I. R. (2019) U-Pb monazite ages of the Kabanga mafic-ultramafic intrusions and contact aureoles, central Africa: Geochronological and tectonic implications. GSA Bulletin, 131, 1857-1870.

725 **Figure captions**

726 **Figure 1** (a) Tectonic division of China showing the Qinling Orogen between the Yangtze and North
727 China Cratons. (b) Sketch geologic map of the South Qinling Belt showing the location of major gold
728 deposits relative to regional faults and granitoid intrusions (modified after Chen et al. 2004, the
729 geochronological data is detailed in the Appendix Table A1 and references therein).

730

731 **Figure 2** (a) Geological map of the Qiuling sediment-hosted gold deposit; (b) Stratigraphic column of
732 the Nanyangshan Formation and Yuanjiagou Formation (modified after Geology of Jinlongshan
733 microscopic disseminated gold deposit in Shaanxi province,1997).

734

735 **Figure 3** (a) Photograph showing the disseminations of pyrite (Py) and arsenopyrite (Apy) in the
736 metasedimentary rock; (b) Backscattered electron image showing the main alteration types of the
737 Qiuling gold deposit, microcrystalline quartz, sericite, and sulfides mainly occur in the side of silty
738 limestone (bedding S_0); (c) Backscattered electron image of zoning monazite (Mnz) crystal; (d) Cut
739 thin section including monazite marked by red spots; (e) Photographs showing the monazite samples
740 used for U-Pb dating; (f) The image of $^{232}Th^{16}O_2$ signals from SIMS.

741

742 **Figure 4** Backscattered electron images showing the textures of monazite (Mnz) occurrences. (a) and
743 (b) The detrital monazites occur in the sedimentary rocks; (c) native gold grain occurs associated with
744 arsenopyrite (Apy); (d-g) Hydrothermal monazite grains coexistence with pyrite (Py) and arsenopyrite;
745 (h) and (i) intergrowths of monazite with pyrite and arsenopyrite. The larger version of each image
746 showing zonations of monazite grains.

747

748 **Figure 5** High-contrast BSE images (a, b), and WDS X-ray maps for two monazite crystals showing
749 element distribution maps for U (c, d), Th (e, f), Ca (g, h), La (i, j), Y (k, l). Note the similarity of
750 distribution patterns for U, Th, Ca, and Y in the detrital cores.

751

752 **Figure 6** (a) La *vs.* Nd plot; (b) Discrimination of monazite with different origins including igneous,
753 metamorphic, and hydrothermal monazite, the arrow arrange was referred from Wu et al. 2019; (c)
754 Ternary diagram of LREE, HREE, and (Th + U); (d) Brabantite $Ca(Th, U)REE_{-2}$ *vs.* huttonite (Th,
755 $U)SiREE_{-1}P_{-1}$exchange in monazite shon in the cationic plot (per formula units for 4 oxygens) of (Th +
756 U + Si) *vs.* (REE + P +Y).

757

758 **Figure 7** Dating results of monazite in the Qiuling deposit. (a) Tera-Wasserburg U-Pb plot for areas
759 with different U contents and common Pb compositions in detrital and hydrothermal monazites; (b)
760 The weighted average ^{207}Pb common Pb corrected $^{206}Pb/^{238}U$ age for hydrothermal monazite
761 (data-point uncertainties are 2σ); (c) Histogram of monazite $^{208}Pb/^{232}Th$ ages. BSE images of
762 representative monazite grains show measured ^{207}Pb corrected common Pb $^{206}Pb/^{238}U$ ages (2σ level);
763 (d) Plot of Th concentrations (ppm) *vs.* $^{208}Pb/^{232}Th$ ages.

764

765 **Figure 8** Age distribution of gold deposits from the South Qinling Terrain gold district. The age data,
766 detailed in the Appendix (Table A1), and this study. The tectonic evolution of the region during the
767 Mesozoic is based upon Wang et al. (2011), Dong and Santosh (2016), Qiu et al. (2018), and Wu et al.
768 (2019) and the references therein.

769

770 **Appendix**

771 Table A1. Age data of gold deposits from the South Qinling Orogen gold district

772

773 Table A2. Analytical conditions of EPMA measurements of monazite

774

775 Table A3. Electron microprobe data of monazite

776

777 Table A4. *In-situ* SIMS U-Th-Pb dating results of M6 monazite standard by 2-μm beam size dating

778

779 Table A5. *In-situ* SIMS U-Th-Pb dating results of muti-type monazites from the Qiuling SHDG deposit

780

781 Table A6. The monazite closely associated with ores in representative sediment-hosted gold deposits
782 worldwide without well-constrained ages.

Figure 1

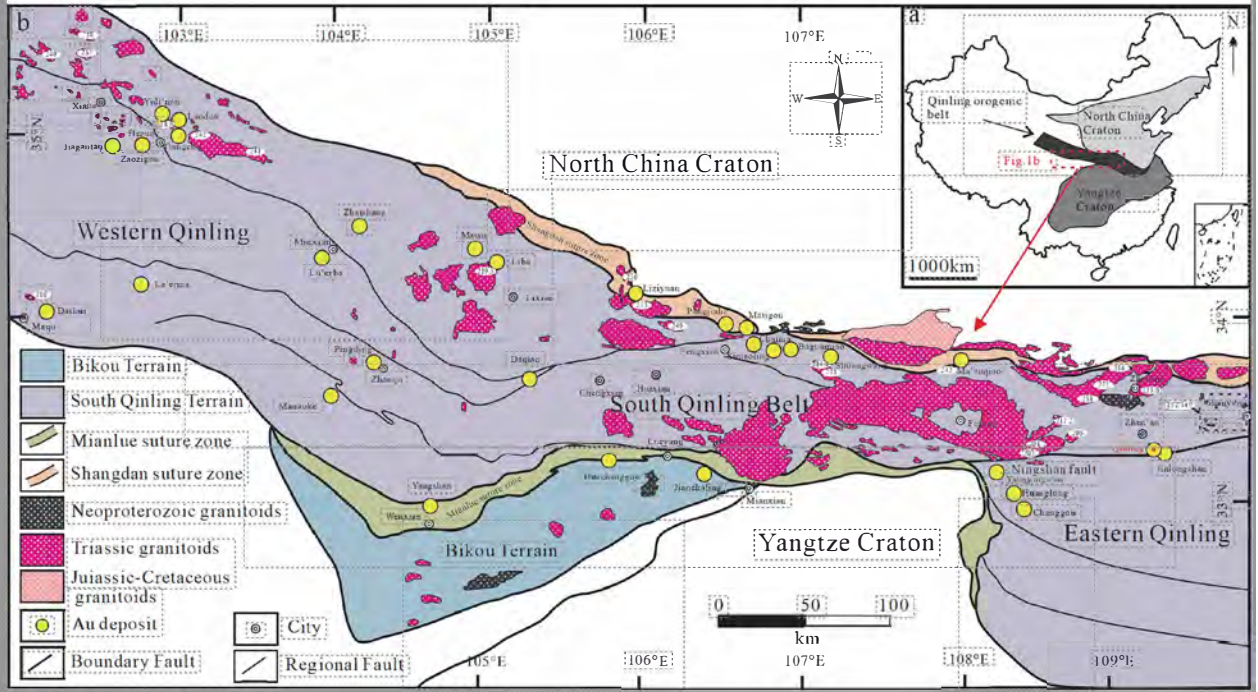
b
103°E
104°E
105°E
106°E
107°E
N
W
E
S
35°N
34°N
33°N
North China Craton
Western Qinling
South Qinling Belt
Bikou Terrain
Yangtze Craton
Eastern Qinling
Ningshan fault
Mianlue suture zone
Shangdan suture zone
Xiahe
Tewo
Luodian
Jiaguanjing
Zaozigou
Zhuxiling
Maoyu
Liba
Taiyangping
Liziyuan
Mengpo
Lueyang
Diqing
Zhenpo
Yangdian
Wenyan
Hanchengping
Jiaochangba
Mianxian
Changpo
Fengjiaba
Zhen'an
Laoyingzhai
0
50
100
km
105°E
106°E
107°E
108°E
109°E
a
N
Qinling orogenic belt
North China Craton
Fig. 1b
Yangtze Craton
1000km
Bikou Terrain
South Qinling Terrain
Mianlue suture zone
Shangdan suture zone
Neoproterozoic granitoids
Triassic granitoids
Juiassic-Cretaceous granitoids
Au deposit
Boundary Fault
City
Regional Fault

Figure 2

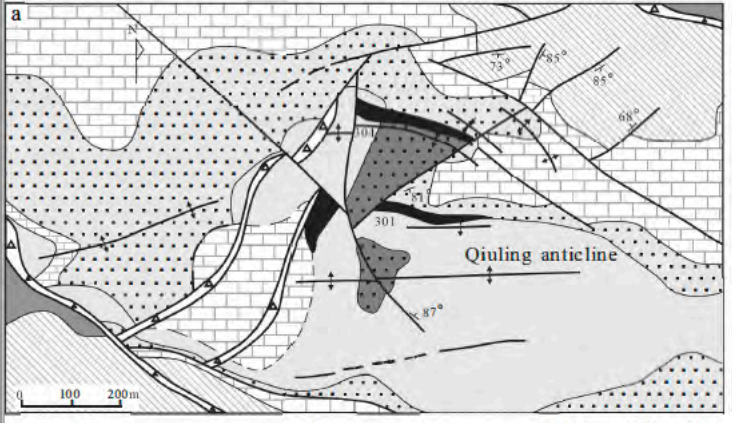

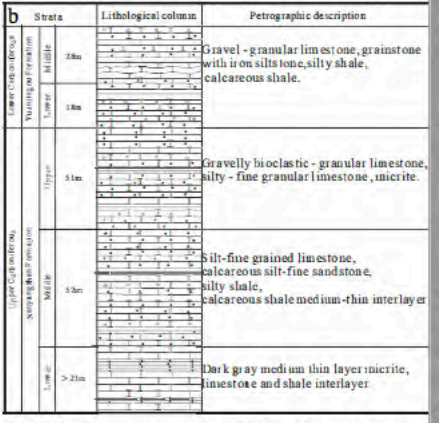

Middle Carboniferous Sixiakou Formation

Lower Carboniferous Yuanjiagou Formation

Upper unit of the Upper Devonian Nanyangshan Formation

Middle unit of the Upper Devonian Nanyangshan Formation

Lower unit of the Upper Devonian Nanyangshan Formation

Upper Devonian Lengshuihe Formation

Stratigraphic Boundary

Fault

Crushed zone

Syncline

Anticline

301 Ore Body and number

Figure 3

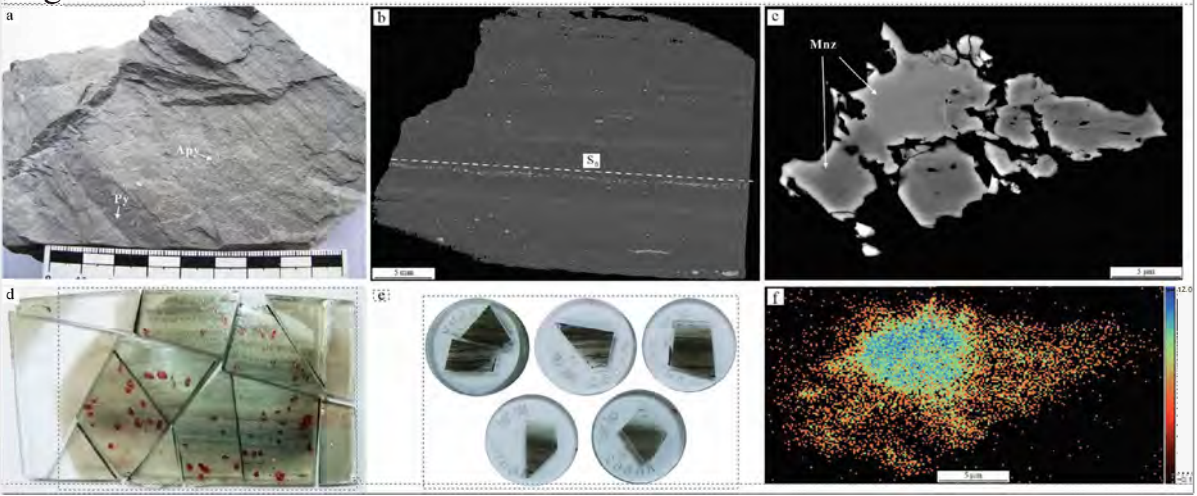

Figure 4

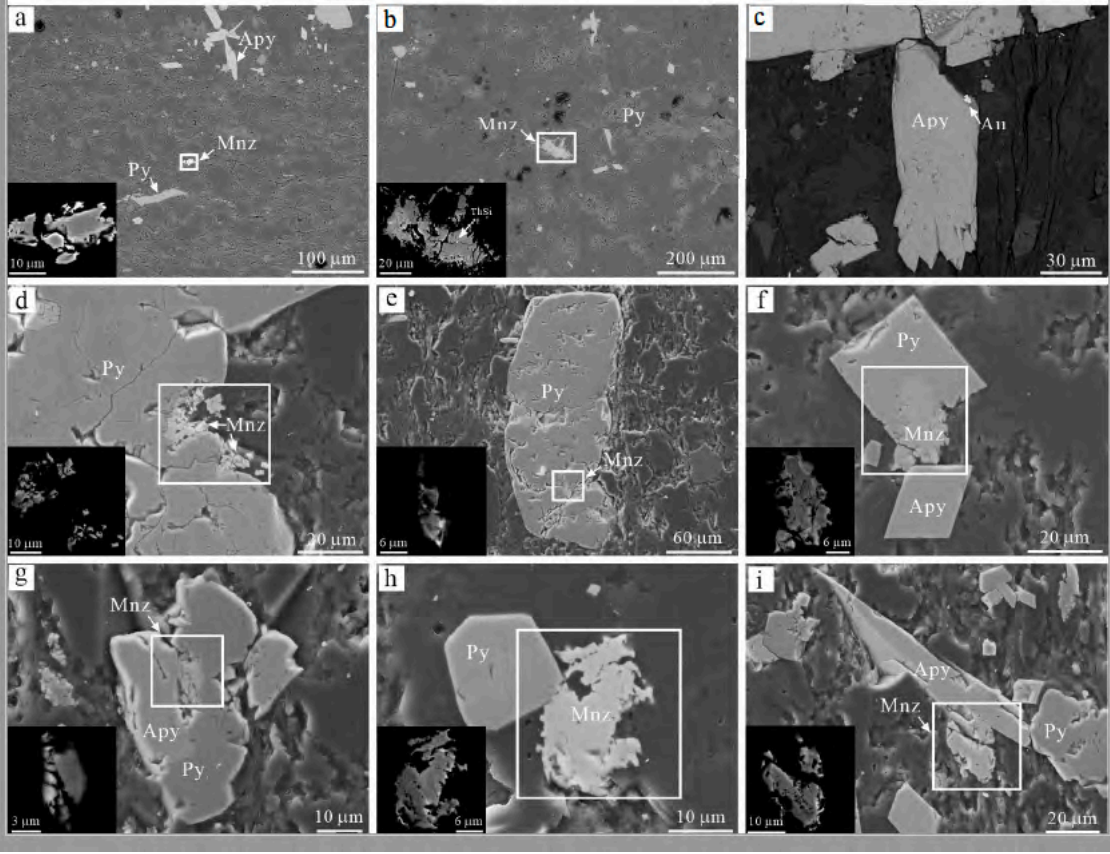
a
Apy
Mnz
Py
10 μm
100 μm
b
Mnz
Py
ThSi
20 μm
200 μm
c
Apy
An
30 μm
d
Py
Mnz
10 μm
20 μm
e
Py
Mnz
6 μm
60 μm
f
Py
Mnz
Apy
6 μm
20 μm
g
Mnz
Apy
Py
3 μm
10 μm
h
Py
Mnz
6 μm
10 μm
i
Apy
Mnz
Py
10 μm
20 μm

Figure 5

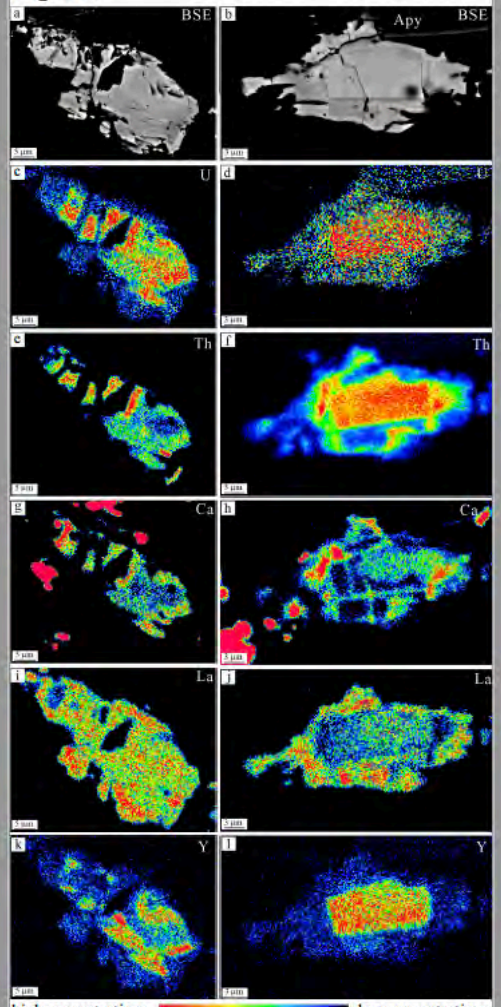
a
BSE
5 µm
b
Apy
BSE
5 µm
c
U
5 µm
d
U
5 µm
e
Th
5 µm
f
Th
5 µm
g
Ca
5 µm
h
Ca
5 µm
i
La
5 µm
j
La
5 µm
k
Y
5 µm
l
Y
5 µm
high concentrations
low concentrations

Figure 6

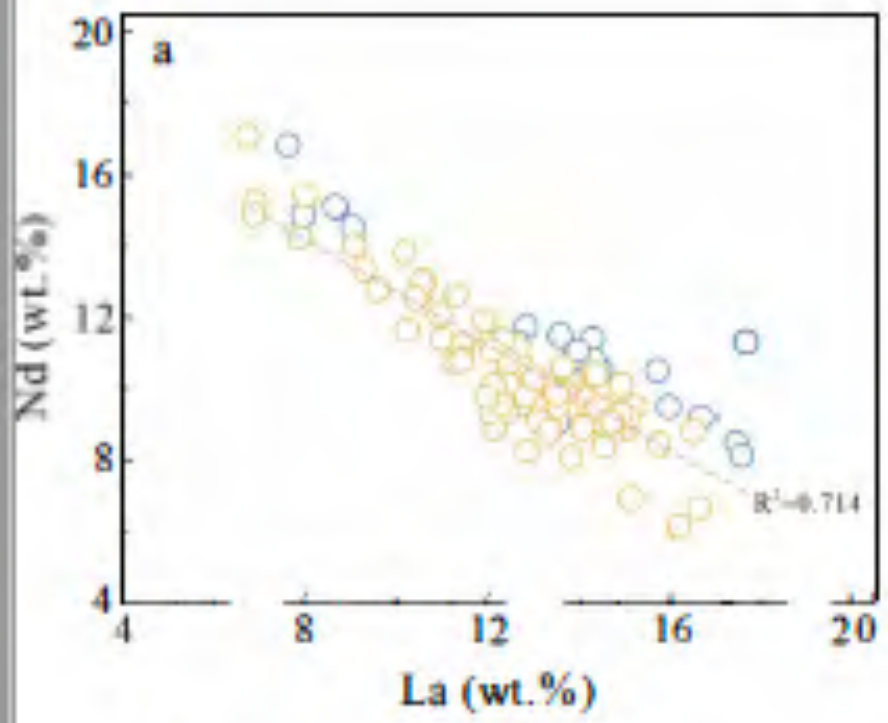
a
Nd (wt.%)
La (wt.%)
20
16
12
8
4
4
8
12
16
20
R²=0.714

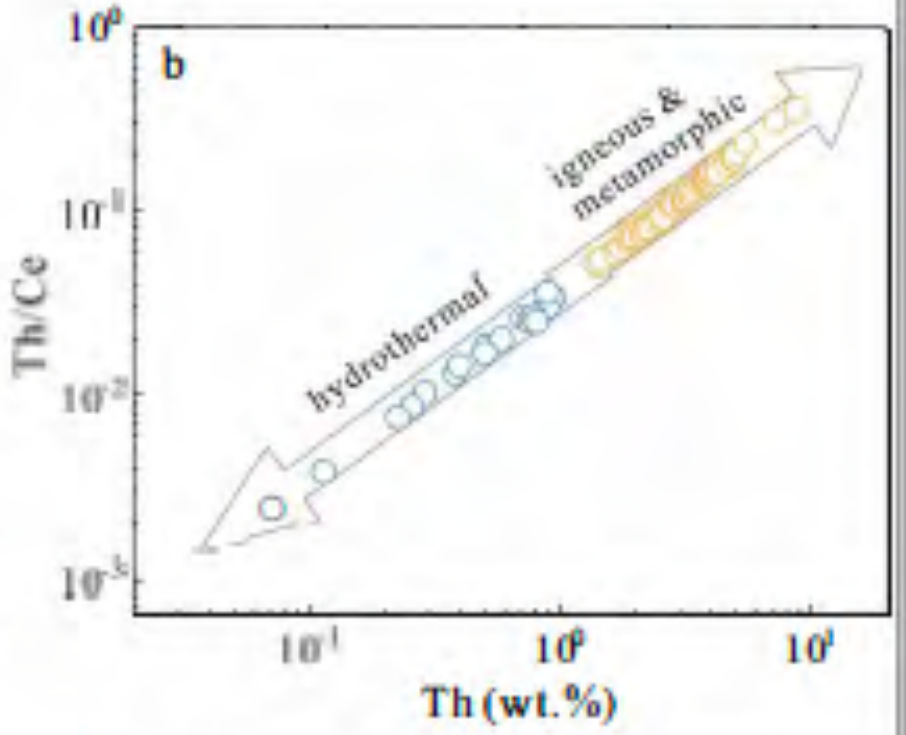
b
Th/Ce
Th (wt.%)
igneous &
metamorphic
hydrothermal

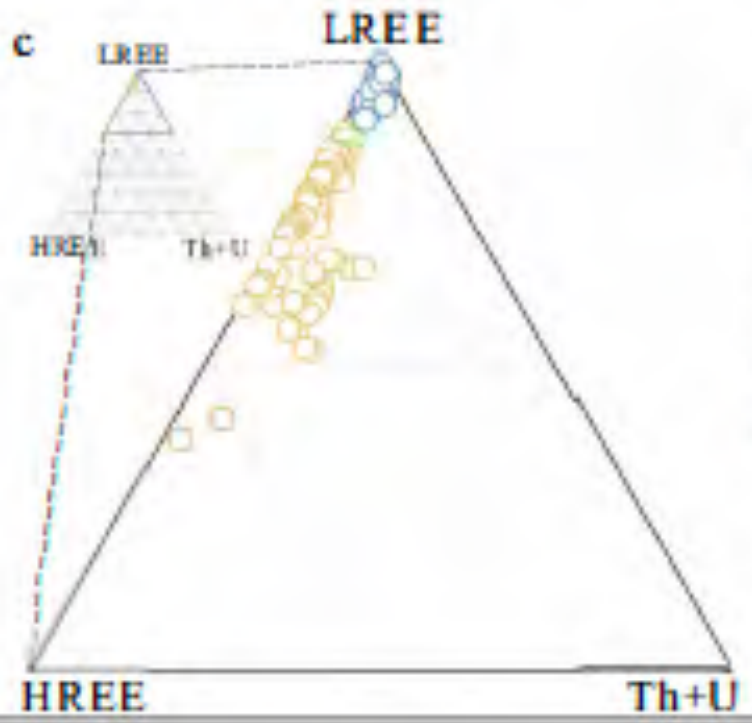
c
LREE
LREE
HREE
Th+U
HREE
Th+U

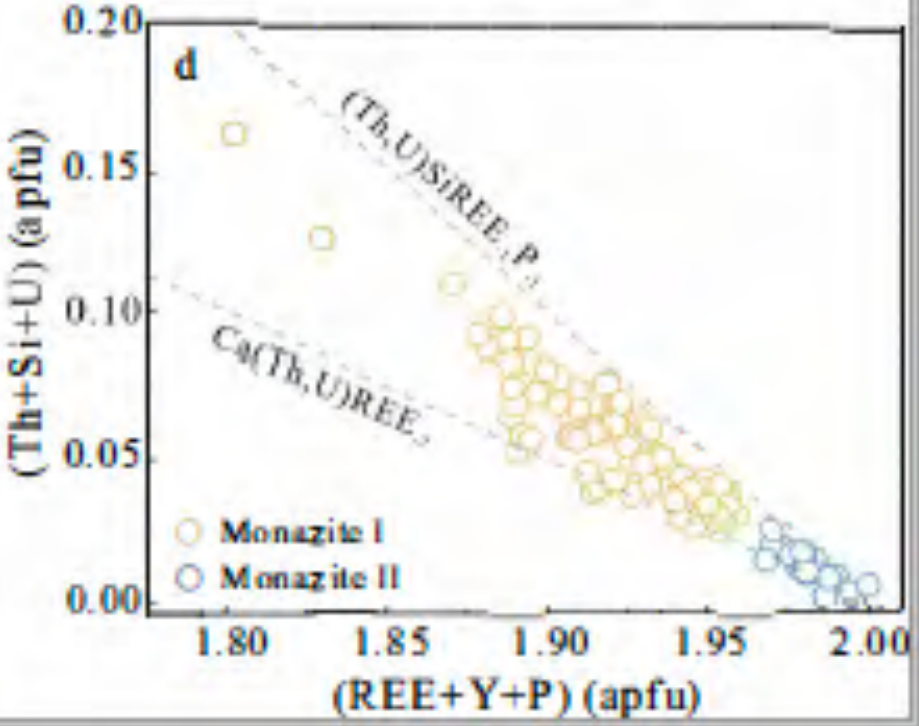
d
(Th+Si+U) (apfu)
(REE+Y+P) (apfu)
(Th,U)SiREE₋₁P₋₁
Ca(Th,U)REE₋₂
Monazite I
Monazite II

Figure 7

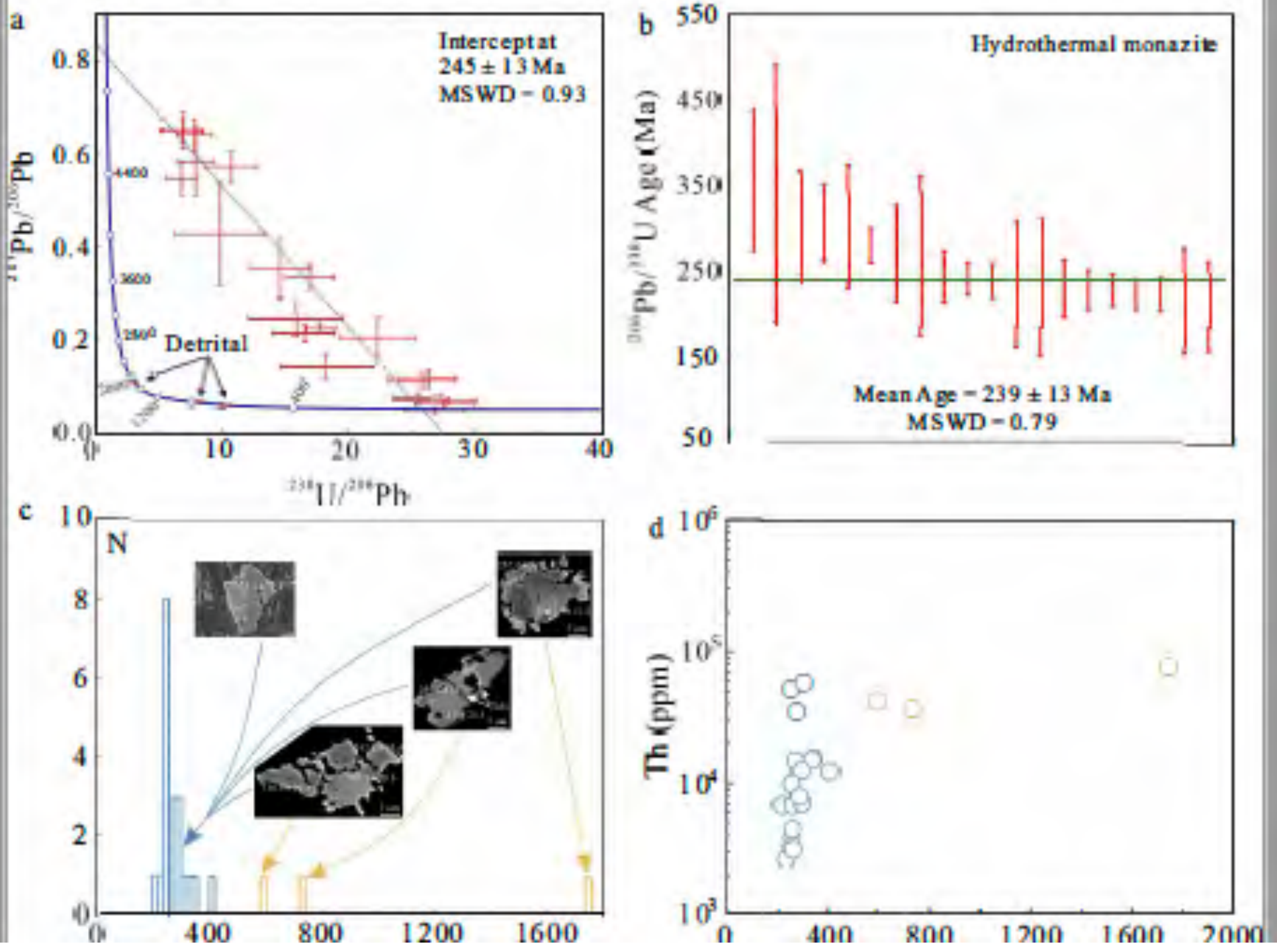
a
Interceptat
245 ± 13 Ma
MSWD = 0.93
Detrital
4400
3600
2800
0.8
0.6
0.4
0.2
0.0
0
10
20
30
40
b
Hydrothermal monazite
Mean Age = 239 ± 13 Ma
MSWD = 0.79
550
450
350
250
150
50
c
N
10
8
6
4
2
0
0
400
800
1200
1600
d
10^6
10^5
10^4
10^3
Th (ppm)
0
400
800
1200
1600
2000

Figure 8

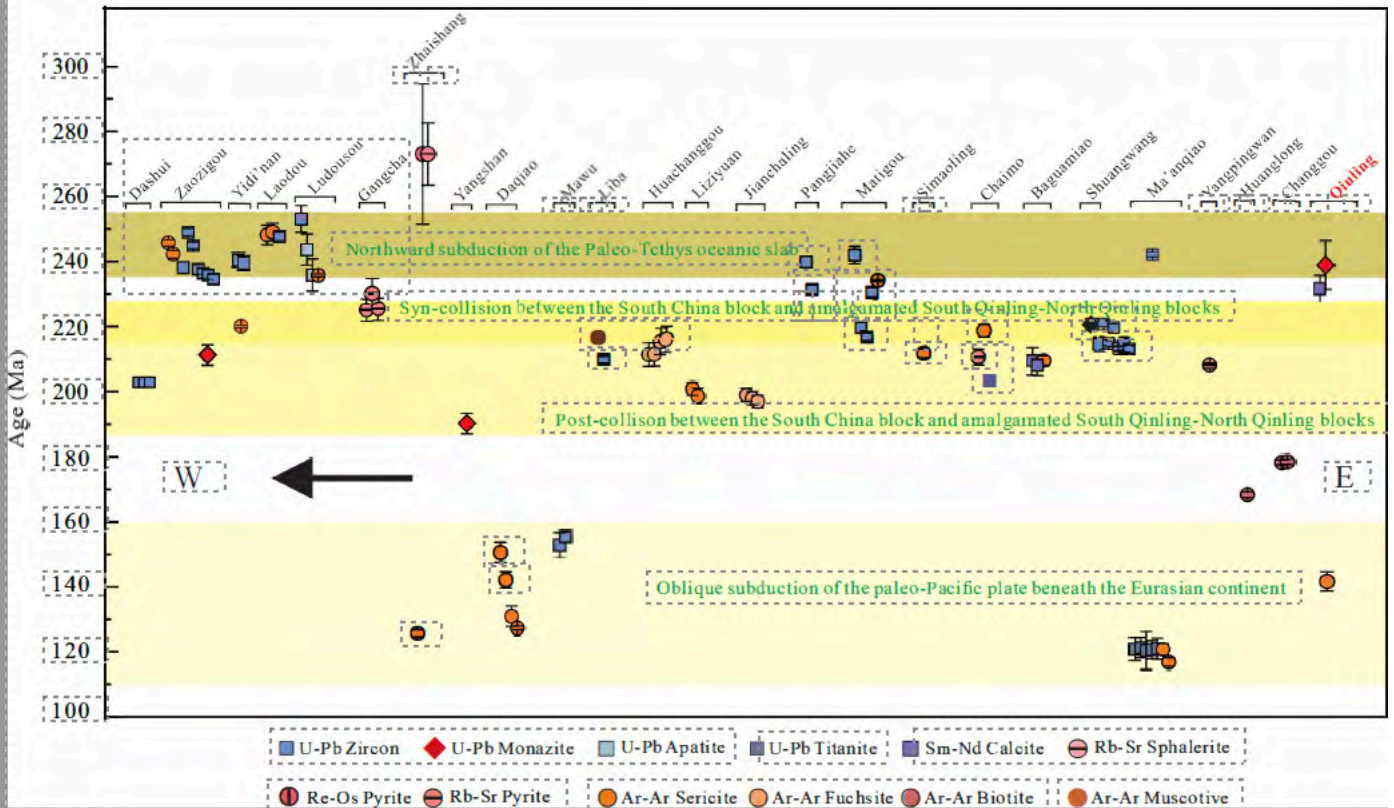
Age (Ma)
300
280
260
240
220
200
180
160
140
120
100
Dashui
Zaozigou
Yidi'nan
Laodou
Ludousou
Gangcha
Zhaishang
Yangshan
Daqiao
Mawu
Liba
Huachanggou
Liziyuan
Jianchaling
Pangjiahe
Matigou
Simaoling
Chaimo
Baguamiao
Shuangwang
Ma'anqiao
Yangpingwan
Huanglong
Changgou
Qinling
Northward subduction of the Paleo-Tethys oceanic slab
Syn-collision between the South China block and amalgamated South Qinling-North Qinling blocks
Post-collison between the South China block and amalgamated South Qinling-North Qinling blocks
Oblique subduction of the paleo-Pacific plate beneath the Eurasian continent
W
E
U-Pb Zircon
U-Pb Monazite
U-Pb Apatite
U-Pb Titanite
Sm-Nd Calcite
Rb-Sr Sphalerite
Re-Os Pyrite
Rb-Sr Pyrite
Ar-Ar Sericite
Ar-Ar Fuchsite
Ar-Ar Biotite
Ar-Ar Muscovite